







# Geometrical feature analysis and disaster assessment of the Xinmo landslide based on remote sensing data


FAN Jian-rong<sup>1</sup>  <http://orcid.org/0000-0003-3426-0751>; e-mail: fjrong@imde.ac.cn

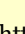
ZHANG Xi-yu<sup>1,2</sup>  <http://orcid.org/0000-0002-1322-9942>; e-mail: zhangxiyu@imde.ac.cn

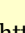
SU Feng-huan<sup>1\*</sup>  <http://orcid.org/0000-0002-7355-5715>;  e-mail: fhsu@imde.ac.cn

GE Yong-gang<sup>1</sup>  <http://orcid.org/0000-0002-8376-7324>; e-mail: gyg@imde.ac.cn

Paolo TAROLLI<sup>3</sup>  <http://orcid.org/0000-0003-0043-5226>; e-mail: paolo.tarolli@unipd.it

YANG Zheng-yin<sup>4</sup>  <http://orcid.org/0000-0001-5366-401X>; e-mail: yangzhengyin1366@163.com

ZENG Chao<sup>5</sup>  <http://orcid.org/0000-0001-7269-8602>; e-mail: zeng3chao@163.com

ZENG Zhen<sup>5</sup>  <http://orcid.org/0000-0002-8168-2570>; e-mail: zengzhen1366@163.com

\* Corresponding author

<sup>1</sup> Key Laboratory of Mountain Hazards and Earth Surface Process, Institute of Mountain Hazards and Environment, Chinese Academy of Sciences, Chengdu 610041, China

<sup>2</sup> University of Chinese Academy of Sciences, Beijing 100049, China

<sup>3</sup> Department of Land, Environment, Agriculture and Forestry, University of Padova, Agripolis, viale dell'Università 16, 35020 Legnaro (PD), Italy

<sup>4</sup> Sichuan Remote Sensing Information, Surveying and Mapping Institute, Chengdu 610100, China

<sup>5</sup> Sichuan Engineering Research Center for Emergency Mapping & Disaster Reduction/Sichuan Geomatics Center, Chengdu 610041, China

**Citation:** Fan JR, Zhang XY, Su FH, et al. (2017) Geometrical feature analysis and disaster assessment of the Xinmo landslide based on remote sensing data. *Journal of Mountain Science* 14(9). <https://doi.org/10.1007/s11629-017-4633-3>

© Science Press and Institute of Mountain Hazards and Environment, CAS and Springer-Verlag GmbH Germany 2017

**Abstract:** At 5:39 am on June 24, 2017, a landslide occurred in the village of Xinmo in Maoxian County, Aba Tibet and Qiang Autonomous Prefecture (Sichuan Province, Southwest China). On June 25, aerial images were acquired from an unmanned aerial vehicle (UAV), and a digital elevation model (DEM) was processed. Landslide geometrical features were then analyzed. These are the front and rear edge elevation, accumulation area and horizontal sliding distance. Then, the volume and the spatial distribution of the thickness of the deposit were

calculated from the difference between the DEM available before the landslide, and the UAV-derived DEM collected after the landslide. Also, the disaster was assessed using high-resolution satellite images acquired before the landslide. These include QuickBird, Pleiades-1 and GF-2 images with spatial resolutions of 0.65 m, 0.70 m, and 0.80 m, respectively, and the aerial images acquired from the UAV after the landslide with a spatial resolution of 0.1 m. According to the analysis, the area of the landslide was 1.62 km<sup>2</sup>, and the volume of the landslide was 7.70 ± 1.46 million m<sup>3</sup>. The average thickness of the landslide accumulation was approximately 8 m. The landslide destroyed a total of 103 buildings. The area

**Received:** 12 August 2017

**Accepted:** 21 August 2017

of destroyed farmlands was 2.53 ha, and the orchard area was reduced by 28.67 ha. A 2-km section of Songpinggou River was blocked and a 2.1-km section of township road No. 104 was buried. Constrained by the terrain conditions, densely populated and more economically developed areas in the upper reaches of the Minjiang River basin are mainly located in the bottom of the valleys. This is a dangerous area regarding landslide, debris flow and flash flood events. Therefore, in mountainous, high-risk disaster areas, it is important to carefully select residential sites to avoid a large number of casualties.

**Keywords:** Xinmo Landslide; Geological disaster; Remote Sensing; Unmanned aerial vehicle (UAV); Digital elevation model (DEM); Satellite data

## Introduction

At 5:39 am on June 24, 2017, a huge landslide occurred in the village of Xinmo in Maoxian County, Aba Tibet and Qiang Autonomous Prefecture, Sichuan Province, Southwest China (Figure 1). The Xinmo landslide was triggered by various factors: the local geologic structure, the instabilities related to the historical earthquakes (e.g. the 1933 M7.5 Diexi earthquake and the 2008 M8.0 Wenchuan earthquake), and the rainfall (Su et al. 2017). This area with steep slope belongs to a gorge-alpine region in the upper reaches of the Minjiang River basin. Also, it was affected by the 2008 Wenchuan earthquake (local earthquake intensity is VII degree at the China seismic intensity scale) (Figure 1a). Moreover, the epicentre of the 1933 Diexi earthquake (103°36' E, 31°54' N) (Wang and Shen 2011) was very close to the location of the Xinmo landslide (103°39'21" E, 32°4'19" N). Several unstable hillslopes, prone to mountain hazards such as landslides, debris flows and flash floods, were generated by strong earthquakes (Xu et al. 2009). According to Xu and Li (2010), 112 large landslides had occurred in the earthquake-stricken area by the year 2010, each of which had a plane area greater than 50,000 m<sup>2</sup>. These landslides provided an abundance of unstable material that serves as the sediment source for debris flows induced by heavy rainfall (Cui et al. 2009; Fan et al. 2010; Cui et al. 2011). For the case of the Xinmo landslide, from 1 to 24, June, the accumulated precipitation ranged from

78 up to 103 mm (Su et al. 2017). The data were obtained from field precipitation stations nearby, which were established by Institute of Mountain Hazards and Environment (Chinese Academy of Sciences). The long duration of rainfall accelerated the expansion of cracks and further triggered the Xinmo landslide (Su et al. 2017).

After the landslide, a map of the main geometrical features is information urgently needed (Guzzetti et al. 2009). An inventory map of such geometrical features (Galli et al. 2008) could be useful for visualizing the disaster (Figure 1b) and helping to prevent secondary disasters. The landslide volume estimation can help for risk assessment of secondary disasters such as debris flows and lake damming. However, although the landslide area is relatively easy to obtain, the volume estimation is a challenge (Fan et al. 2012; Jaboyedoff et al. 2012; Schlögel et al. 2015; Stumpf et al. 2015). Acquiring the length, width and average thickness of the landslide deposit is a commonly used method to calculate the volume of the landslide deposit. The length and width can be acquired from on-site measurements or remote sensing image interpretation. The average thickness is often obtained by drilling or estimated by the first-hand experience. The accuracy of the volume obtained by these methods depends on the estimation accuracy of the average thickness. Calculation of landslide volumes is more accurate for deposits that have been investigated on-site, where the average thickness is measured by drilling (Fan et al. 2011). In most cases, such info is estimated by the first-hand experience, and the accuracy of the volume calculated by this method is relatively low.

In the last few years, high-resolution topography data from Light Detection and Ranging (LIDAR) (Jaboyedoff et al. 2012; Tseng et al. 2013; Passalacqua et al., 2014; Tarolli 2014) or aerial photogrammetry (Lucieer et al. 2014; Turner et al. 2015) has been widely used to analyze and extract landslide geometrical features (DeLong et al. 2012; Tarolli et al. 2012; Lin et al. 2013; Tseng et al., 2015; Tseng et al. 2017). When a landslide occurs, the vegetation and buildings are often covered by debris according to the field investigation pictures and the remote sensing images. Therefore, the thickness of the deposits can be obtained if a digital elevation model (DEM) of the area before the

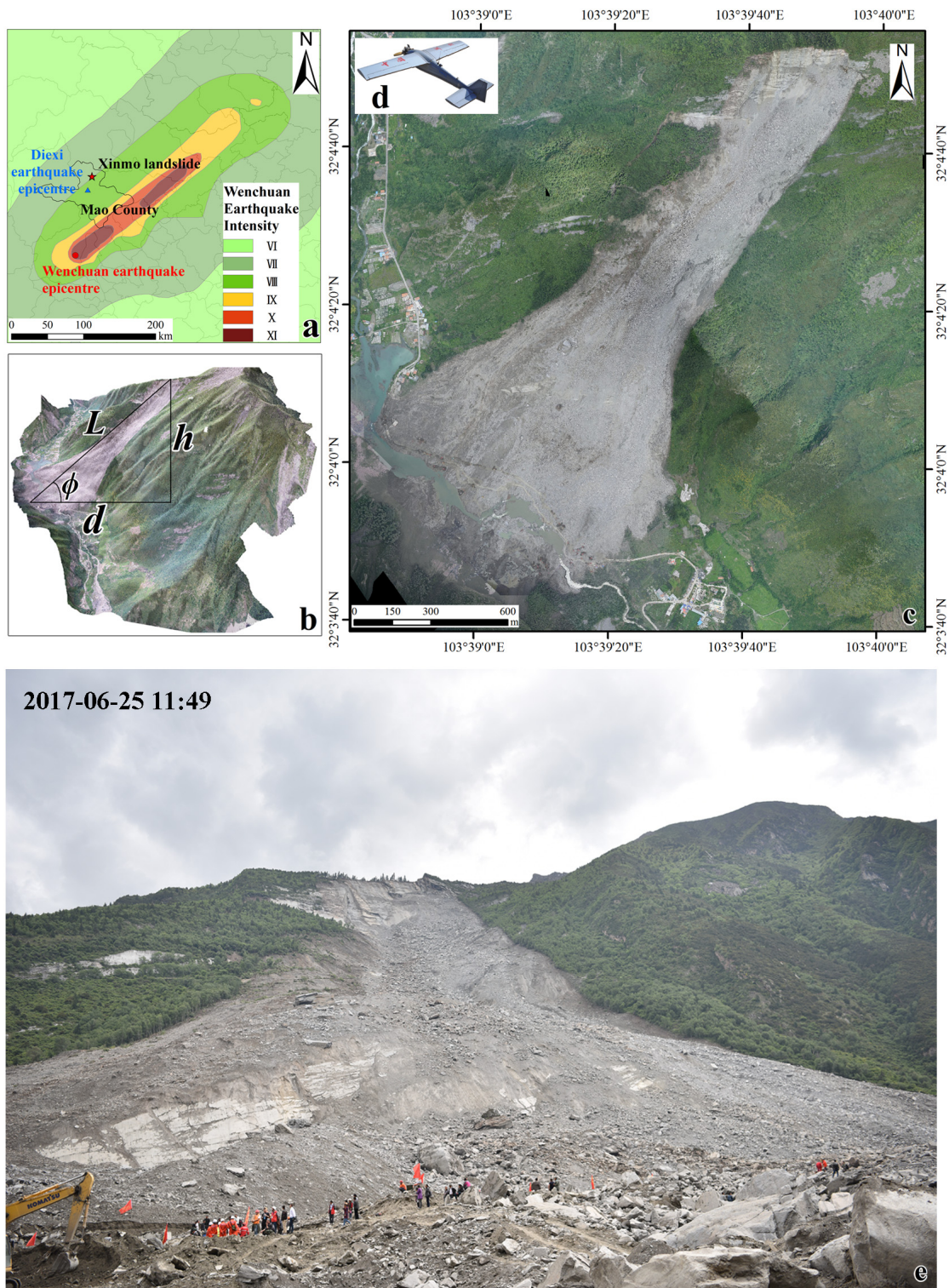


**Figure 1** Location of the Xinmo landslide. a) Xinmo landslide occurred in the affected area of the Wenchuan earthquake (local earthquake intensity is VII degree at the China seismic intensity scale), and very close to the epicentre of the 1933 Diexi earthquake. b) 3D model of the Xinmo landslide,  $L$  is the landslide length (m),  $h$  is the landslide height (m),  $d$  is the landslide horizontal sliding distance (m), and  $\phi$  is the apparent friction angle ( $^{\circ}$ ). c) The aerial image after the landslide. d) The unmanned aerial vehicle (UAV) used in this study. The UAV was designed and assembled by Sichuan Bureau of Surveying, Mapping and Geo-information (SBSMG), weighs less than 10 kg, and can fly for up to 4 hours. e) Rescue site photo provided by WANG Jiao from the Institute of Mountain Hazards and Environment (CAS).

landslide is available. Another commonly used method for estimating the volume of a landslide deposit is by the empirical statistical model (Rice et al. 1969; Innes 1983; Guthrie and Evans 2004; Korup 2005; Imaizumi et al. 2008; Fiorucci et al. 2011; Fan et al. 2012). For large-area surveys, the volume of the landslide deposit is estimated by the relationship between the volume and the area affected. Also, a statistical model for a single landslide can be used to estimate the volume of the landslide material (Fan et al. 2011).

In addition to the landslide geometrical features, the disaster assessment is a necessary step to plan suitable emergency responses and to reduce casualties (Guzzetti et al. 1999; Calò et al. 2014; Santangelo et al. 2015). In the mountainous region of Southwest China, the terrain and climate provide conditions to mountain hazards occurrence (Wang et al. 2009). There the disaster assessment is difficult to carry out with traditional methods which take considerable time, manpower and material resources. However, it must be completed quickly for emergency responses to reduce casualties (Fan et al. 2016). Therefore, remote sensing technology is becoming a very useful approach for such investigation.

The main goal of this paper is to present an analysis of the spatial distribution of thickness, volume, topographic change, unstable mass characteristics, and disaster assessment. The analyses are based on change detection of remote sensing data. The obtained results should provide a reference for rescue and reconstruction.

## 1 Materials and Methods

### 1.1 Data sources

Sichuan Bureau of Surveying, Mapping and Geo-information (SBSMG) collected the digital terrain data (2013 pre-event and 2017 post-event DEM) used to obtain the surface and subsurface geometry of the landslide accumulation. On June 25, aerial images with a spatial resolution of 0.1 m were acquired by SBSMG through a UAV survey. Remote sensing satellite images, obtained before the landslide from the QuickBird, Pleiades-1 and GF-2 satellites were also collected for the disaster assessment (Table 1). The spatial resolution of the

**Table 1** Remote sensing image data before and after the Xinmo landslide

Date	Source	Spatial resolution (m)	
		Multi-spectral	Pan
2003	QuickBird	2.62	0.65
2013-01-17	Pleiades-1	2.80	0.70
2017-04	GF-2	3.20	0.80
2017-06-25	UAV aerial images	0.10	-

remote sensing data has a significant influence on the assessment of the disasters (Fan et al. 2010). Since the panchromatic images possess spatial resolution below 1 m, these satellite images assured a suitable analysis of the damaged buildings. Moreover, six ground control points (GCPs) were used in this study to rectify the remote sensing image data and ensure the accuracy of the estimation of the landslide volume.

### 1.2 Aerial photographs and DEM collected after the landslide event

Aerial photogrammetry using UAV surveying (Nex and Remondino 2014; Smith and Vericat 2015) is time efficient and cost effective in comparison with other traditional land survey methods in most of the mountainous areas (Koi et al. 2008). The aircraft used in this study, which is a fixed-wing UAV (Figure 1d), was designed and assembled by SBSMG, weighs less than 10 kg, and can fly for up to 4 hours. Color photos (0.1 m spatial resolution) were acquired by UAV using a Nikon D800E camera equipped with a 36 mm lens. On June 25, the UAV conducted 3 flights, and a total of 824 photos were taken. The acquired aerial photos had adequate overlap with the adjacent photos, and the distorted or blurred photos were eliminated from the dataset. The photos were processed using the IPS (Icaros Photogrammetric Suite) software (<https://www.icaros.us/ips-software>). The interior orientation was determined from the metadata to align the photos, build geometry and build texture (Nex and Remondino 2014). The processed data served as the basis to generate a 3D point cloud, a DEM and a digital orthophoto map (DOM). The GPS system onboard the UAV recorded the flight track data that was used for georeferencing by the simultaneity of the GPS time and the camera inertial time. However, the GPS system onboard the aircraft might not deliver precise results (Siebert and Teizer 2014).

Therefore, six GCPs were used to guarantee the positioning accuracy. The GCPs were established and measured before the flight using a Real Time Kinematic (RTK) GPS receiver. The accuracy of the RTK GPS receiver used in this study is  $1 \text{ cm} \pm 2$  parts-per-million (ppm) horizontally and  $2 \text{ cm} \pm 2$  ppm vertically. After the adjustment with GCPs, the latitude and longitude of any point on the produced DEM and DOM accurately corresponds to the true coordinates. Two types of post-landslide DEM were processed from the aerial photogrammetry by IPS, and the linear interpolation algorithm was used to convert the 3D point cloud data to the DEM. One DEM was calculated with a spatial resolution of 1 m and a vertical error of 0.6 m, while the other with a spatial resolution of 5 m and a vertical error of 3 m. The DEM of 2013 was obtained through aerial photogrammetry technique at a spatial resolution of 5 m using the linear interpolation algorithm (the vertical error is similar to the DEM obtained at 5 m after the landslide). This is the most recent and highest resolution terrain data available before the landslide. For the analysis, we considered for both DEMs the resolution of 5 m.

### 1.3 Estimation of the thickness and volume of the landslide accumulation

High-resolution terrain data provide the basis for a more accurate extraction of landslide geometrical features (Tarolli et al. 2012). Among the geometrical features of the landslide, the area can be calculated by interpretation of the DOM after the landslide. The destruction of the vegetation and buildings in the images were evident. A visual interpretation was used to identify the boundary of the landslide on the DOM after orthorectification, and the area was obtained accordingly. In addition, the front and back edges were interpreted from the DOM, and then the elevation information was determined from the DEM after the landslide. The horizontal sliding distance was inferred from the DOM and the terrain information provided by the DEM (Figure 1b). However, to estimate the precise volume of the landslide, the surface and subsurface geometry were indispensable. The volume of the landslide was estimated by comparing DEM pre-event and DEM post-event at 5 m. Such analysis was carried

out using the Geomorphic Change Detection 6.1.14 (GCD 6.1.14) toolbar embedded in an ESRI® add-in for ArcGIS 10.X. This toolbar estimates the landslide volume from the change in the digital surfaces, while considering the propagated errors of both the DEMs (Wheaton et al. 2010). A slope surface was categorized as “cut” if material was removed, or identified as “fill” if material was added to the area (Fang et al. 2010). Therefore, the volume of the landslide material was calculated by adding the total net loss and the total net gain separately (Prosdocimi et al. 2015). Similarly, the thickness distribution was obtained from the difference between the DEM after the landslide and the DEM before.

### 1.4 Assessment of the disaster area affected by the Xinmo landslide

After orthorectification of the remote sensing images, the QuickBird images from 2003, the Pleiades-1 images from 2013 and the GF-2 images from April 2017, acquired before the landslide, were used to investigate the land cover. The DOM was used to determine the disaster area. Because the spatial resolution of these images was smaller than 1 m, the houses, farmlands, orchards, roads and rivers were clearly distinguished. The images were first interpreted by supervised classification and then checked by visual interpretation. The spatial resolutions of the three different datasets were in the same order of magnitude (0.65 m, 0.70 m and 0.80 m), therefore the interpretation results of them could be comparable. The analysis was conducted for each image, and the results were converted to a shapefile in ArcGIS. Then, we compared the land cover in the landslide area in four periods: 2003, 2013, 2017 before the landslide, and 2017 after the landslide (Figure 2).

## 2 Results and Discussion

### 2.1 The geometrical features of the Xinmo landslide

The geometrical features of the Xinmo landslide are shown in Table 2. The height of the landslide was 1,103 m, which is the difference between the front edge elevation and the back edge

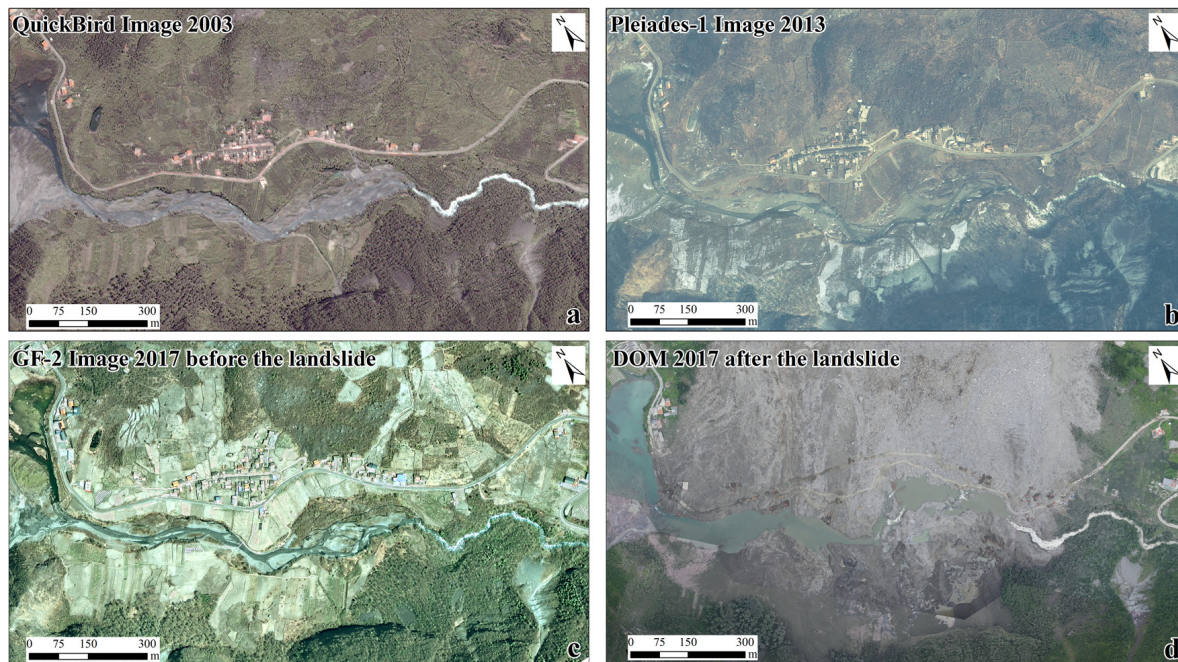


**Figure 2** Land cover in the landslide area in four periods: a) 2003 (QuickBird), b) 2013 (Pleiades-1), c) 2017 before the landslide (GF-2), and d) 2017 after the landslide (digital orthophoto map (DOM)). The scale and position are the same.

elevation. The rear edge and the right edge of the landslide crown (in reference to the direction of movement) were the main fracture surface of the landslide, which were where fissures developed. Due to apparent fissures on the bedrock, the irregular jagged rear edge of the landslide crown was very high and steep. The natural channel below the source area constituted the scraping area of the landslide debris flow, with an average width of 400 m and a length of 700 m. As seen from Figure 3, both sides of the slope in the scraping area were scoured by a rock mass that moved downhill very fast. This observation indicates that the main slip material from the source area had a high kinetic energy and was directed toward the lower part of the slope, along the scraping area, at a very high velocity. From the morphological point of view, the accumulation area of the front of the landslide is fan-shaped, with debris flow accumulation characteristics. The longitudinal section of the landslide, A-A' (Figure 3) had a length of approximately 2.4 km. The material in the accumulation area had an obvious dividing line (Figure 3d) that was a dark gray tone in the DOM. The material in the L3a area was mainly composed of fine particulate matter, while the material in the L3b area was dominated by coarse particles of rock.

**Table 2** The geometrical features of the Xinmo landslide

Geometrical features	Data
Area	1.62 km <sup>2</sup>
Front edge elevation	2325 m above sea level
Back edge elevation	3428 m above sea level
Height	1103 m
Maximum horizontal sliding distance	2418 m
Length	Approximately 2658 m
Maximum width	1200 m

## 2.2 The volume of the landslide accumulation

The volume estimated from the DEM pre and post-event comparison was  $7.70 \pm 1.46$  million m<sup>3</sup>, and the absolute error was 18.96%. The error is due to the vertical error (3 m) and the relatively low spatial resolution (5 m) of considered DEMs. However, sometimes even terrain data with a spatial resolution of 5 m cannot be completely collected before and after landslides in alpine regions. In such cases, the empirical model should be an effective way to provide a preliminary estimation of the volume of the landslide, because correlations between landslide volumes and other

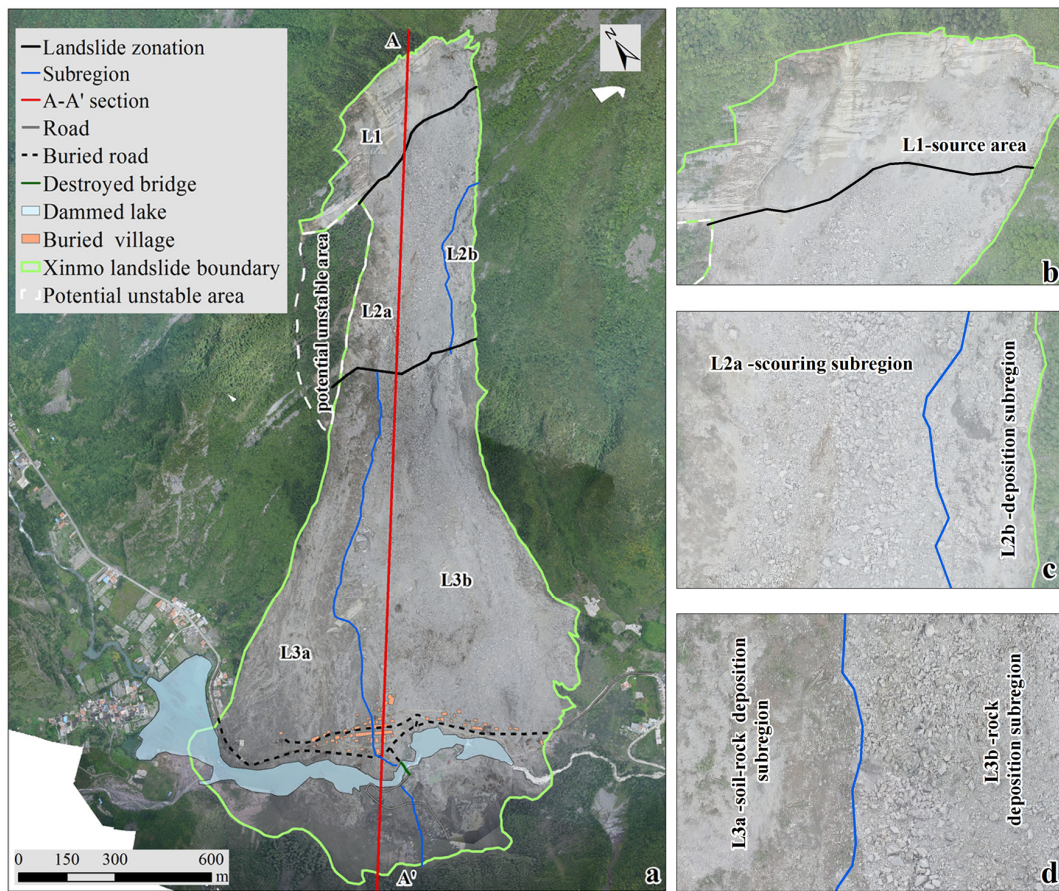


**Figure 3** a) Landslide zonation. b) The steep source area (L1) with fissures on the bedrock. c) The natural channel below the source area, which contained the scouring subregion (L2a) and the deposition subregion (L2b). d) The material of the accumulation area had an obvious dividing line between the soil-rock deposition subregion (L3a) and rock deposition subregion (L3b).

geometrical features are available. For example, the volume of the Xinmo landslide, estimated by the model of Fan et al. (2011) showed by the equation 1, was 8.49 million m<sup>3</sup>. This result is in line with the estimation result using the GCD 6.1.14 toolbar (Wheaton et al. 2010).

$$V_h = e^{2.3869} A_{\perp}^{1.2293} (\tan \phi)^{0.2809} h^{-0.2381} \quad (1)$$

where  $V_h$  is the landslide volume (10<sup>4</sup> m<sup>3</sup>),  $A_{\perp}$  is the landslide projected area (10<sup>4</sup> m<sup>2</sup>),  $\phi$  is the apparent friction angle (°), and  $h$  is the landslide height (m), which is the difference between the front edge and the back edge elevation (Figure 1b).

In most mountainous areas of Southwest China, 5 m DEMs are not available because the altitude is too high to provide a suitable survey through high-resolution terrain data. Therefore, the only terrain data available have low resolutions, such as the ASTER GDEM V2 data with a spatial

resolution of 30 m and a vertical error of 8.3 m (Tachikawa et al. 2011). In this case, the estimation of the volume using the DEM before and after the landslide may not be appropriate due to the large error. Moreover, accurate estimation of landslide volumes requires detailed investigations, including the on-site measurement and digital terrain models with higher resolutions (e.g., 1 m pixel size or less). These methods are very expensive if a large number of landslides occurred simultaneously (in a short period of time) at a large regional scale. For such specific cases, an empirical model can be a feasible method.

### 2.3 The thickness distribution of the landslide accumulation

The thickness distribution was obtained from the difference between the DEM pre and post-event. The thickness distribution is shown in Figure 4.

The average thickness of the landslide accumulation was approximately 8 m, and the local maximum thickness reached 32 m. The accumulation area of the concentrated area in the village of Xinmo ranged from 5 to 10 m, and the partial thickness ranged from 10 to 15 m. The mean thickness of the buried river ranged from 10 to 15 m, with a local maximum thickness of more than 20 m.

### 2.4 The unstable mass characteristics

In the process of extracting the geometrical features of the landslide, it was found that there was a potential unstable mass approximately 500 m below the back edge of the landslide (Figure 5). The geometric parameters of such mass are as follows: surface area of 170,000 m<sup>2</sup>, top elevation

of 3,100 m asl, elevation at the slope foot of 2,650 m asl, maximum width of 300 m, perimeter of 1,700 m, fracture width ranging between 4 to 10 m, fracture length of approximately 900 m, average thickness of approximately 20 m, volume of approximately 3.5 million m<sup>3</sup>, and slope greater than 35 degrees (Table 3). This is a preliminary analysis affected by uncertainties since the volume was calculated from the surface area multiplied by the average thickness. This analysis should, however, be very useful to recognize unstable areas and prevent secondary disasters. At present, the unstable mass deformation could be prone to creating a secondary landslide in the future (Ouyang et al. 2017), because the friction force necessary to commence sliding will decline as a result of the rainwater infiltration and erosion of the slope foot.

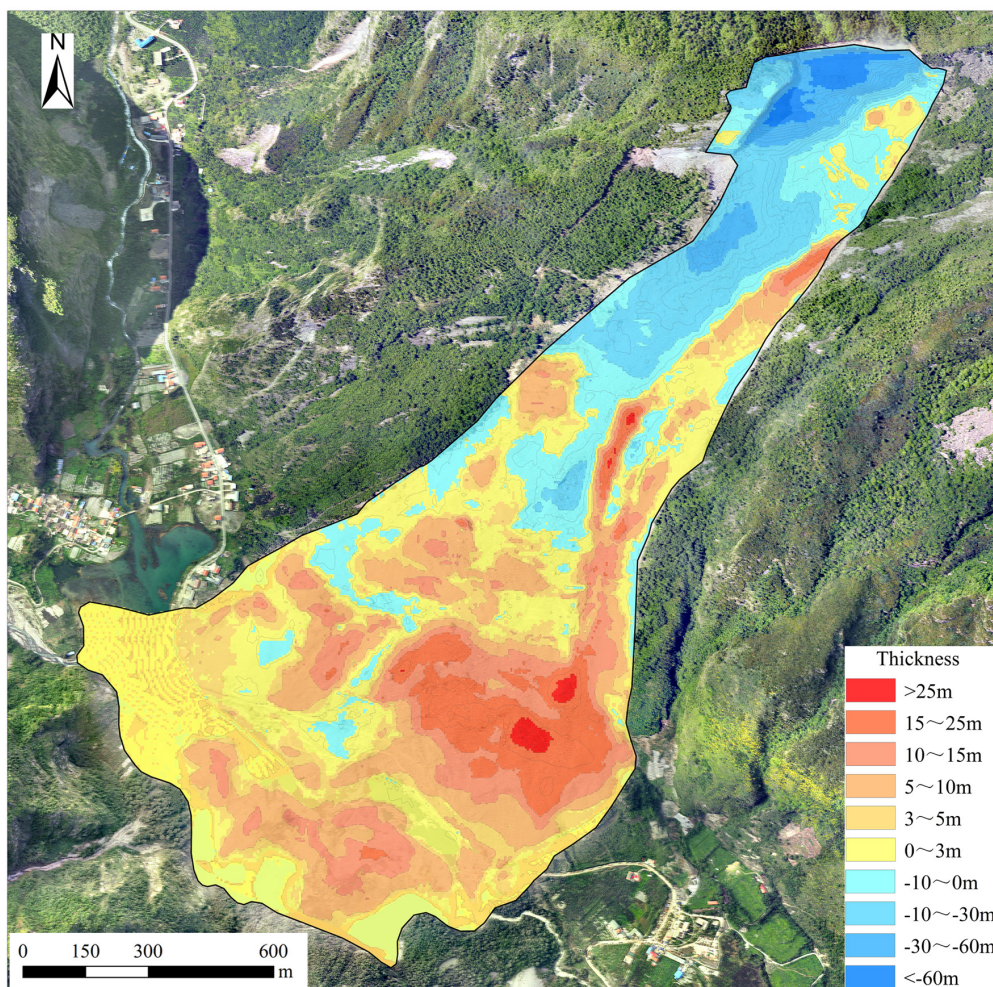


**Figure 4** The thickness distribution of the landslide accumulation. The average thickness of the landslide accumulation was approximately 8 m, and the local maximum thickness reached 32 m.



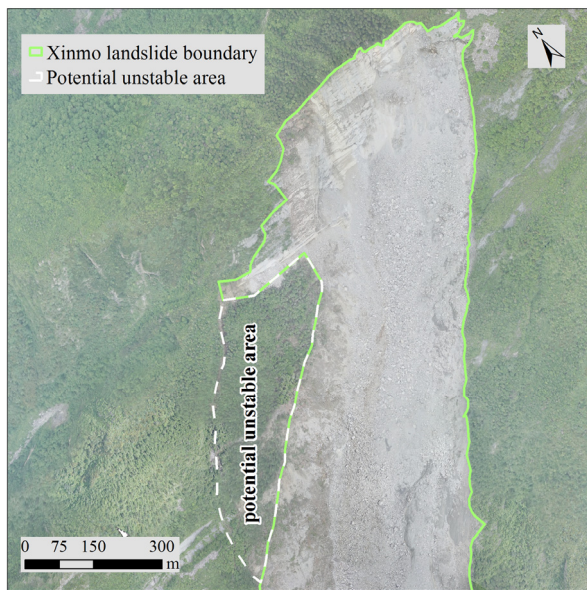


**Figure 5** A potential unstable area approximately 500 m below the back edge of the landslide.

**Table 3** The basic parameters of the unstable mass

Parameters	Data
Surface area	170000 m <sup>2</sup>
Top elevation	3100 m above sea level
Elevation at the slope foot	2650 m above sea level
Maximum width	300 m
Perimeter	1700 m
Fracture width	Between 4 to 10 m
Fracture length	Approximately 900 m
Average thickness	Approximately 20m
Volume	Approximately 3.5 million m <sup>3</sup>
Slope	Greater than 35 degrees

### 2.5 The disaster assessment

The QuickBird images from 2003 (Figure 6), the Pleiades-1 images from 2013 and the GF-2 images from before the landslide (April 2017) were compared to analyze the temporal changes of the buildings (Figure 7). The Xinmo village was located in the landslide accumulation area with a gentle slope below 2310 m above sea level: from 2003 to 2013, the area of the buildings increased from 7576.6 m<sup>2</sup> to 9062.2 m<sup>2</sup>; from 2013 to 2017, the area of the buildings was approximately unchanged. With the increase in the construction area, the disaster risk in the village of Xinmo considerably increased. The landslide destroyed a total of 103 buildings. The affected area was approximately 0.8 km<sup>2</sup>. The area of the destructed farmlands was 2.53 ha, and the orchard area was reduced by 28.67 ha.

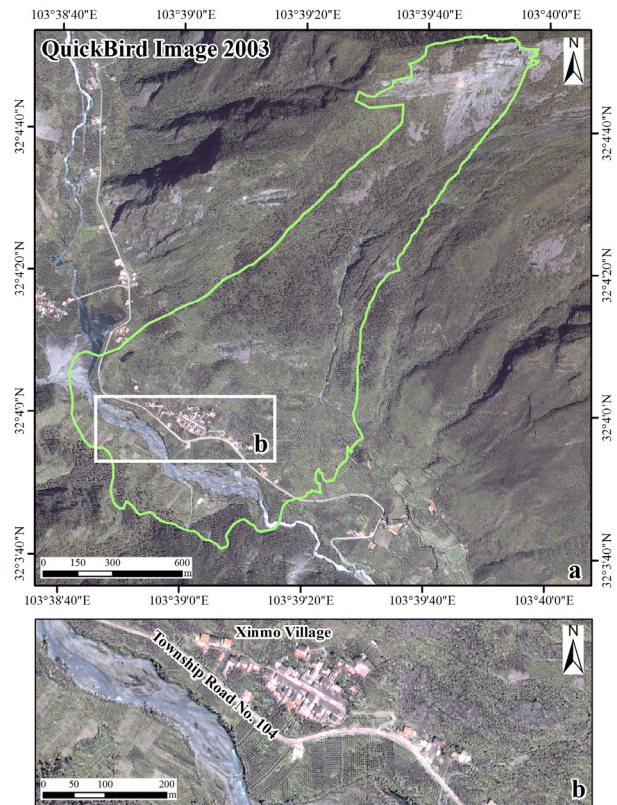


**Figure 6** The QuickBird views of the landslide area (a) and the Xinmo village (b) in 2003.

A 2.1-km section of township road No. 104 was buried and one bridge was destroyed. A 2-km section of Songpinggou River, the first-order tributary of Minjiang River, was blocked and the original river was significantly diverted due to the terrain of the valley and the influence of the landslide accumulation.

Tourism and agriculture of the mountainous region of Southwest China, including the Xinmo landslide area that is located in the upper reaches of the Minjiang River basin, has been rapidly developing in recent years (Fang et al. 2014). The steep slopes have made the traffic less developed in this region than the plains region of Eastern China. However, the alpine ecosystem in Southwest China provides a beautiful mountain scenery. This is a rich resource for the tourism industry. Therefore, tourism and agriculture are the main income sources for the local people, while industry and commerce are less developed. Constrained by the terrain conditions in the mountainous region, the roads, settlements, farmlands, orchards, and so on are densely located in the bottom of the valleys

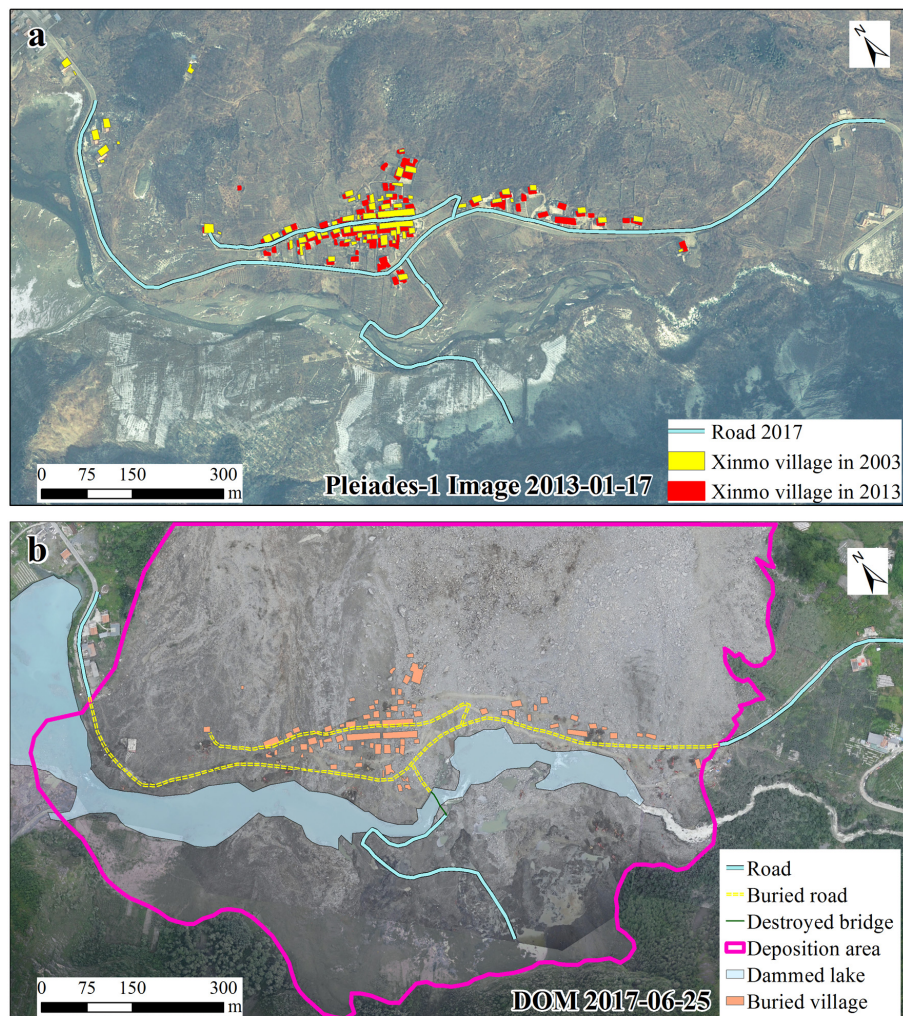


**Figure 7** a) The orthorectified Pleiades-1 image before the landslide (January 17, 2013) and b) the digital orthophoto map (DOM) after the landslide (June 25, 2017) with the same scale and position.

near a gully or river with relatively flat terrain and more suitable transportation conditions. As a result, the bottom of the valleys are densely populated and more economically developed than other areas such as the hillslopes and hilltops. However, the bottom of the valleys are the natural deposition areas of landslides and potentially have a high risk. Therefore, landslides that occur in the mountainous areas of the upper reaches of the Minjiang River basin often cause significant losses, and the rescue and post-disaster reconstruction are very difficult. For example, the village of Xinmo had 40 houses (with over 100 inhabitants) before the landslide. However, as of June 27 at 10 am, a total of 10 deaths were found, and 73 people were still lost. Moreover, with the increase in population in recent years, there is less safe land available for

agriculture and residential buildings. The city of Zhouqu was constructed as a large concentrated residential area on the existing alluvial fan in the Bailong River Valley, which is a tributary of the Jialing River in the Yangtze River Basin. On August 7, 2010, a disastrous debris flow occurred in Zhouqu, and a massive amount of debris and sediment was deposited into the valley. This debris flow caused many casualties; there were 1557 deaths, and 284 people were lost (Tang et al. 2011). Therefore, it is important that we carefully select residential sites in mountainous areas to avoid a large number of casualties due to landslides and other disasters. Construction must suit the local circumstances. The settlements in the bottom of the valleys of the Minjiang River and other rivers in Southwest China should keep the traditional

characteristics of the residents. This includes scattered and multi-point residences, and not large concentrated residential areas.

### 3 Conclusions

In this paper, pre and post-event digital terrain data acquired from aerial surveying were used to analyze the surface and subsurface geometry of the Xinmo landslide. Geometrical features such as the area, volume and the spatial distribution of the thickness of the landslide were calculated. The extraction of the geometry features provided the basis for the disaster assessment and data for the quantitative estimation of landslide volume. This information is vital for emergency response and to prevent secondary disasters. High-resolution terrain data have become an important data source for studies of post-disaster emergencies and terrain changes at watershed scale. However, in most mountainous areas of Southwest China, such data are not available because the altitude is too high to provide a suitable survey. In these cases indeed, the estimation of the landslide volume by comparison of the DEMs before and after the event with relatively low resolution (for example, ASTER GDEM data) may not be appropriate because of the large error. Therefore, an empirical model can be used as an effective and fast preliminary approach to estimate the landslide volume (Fan et al. 2011). The results suggested that the volume estimated using such model is in line with the volume estimated using pre and post-event DEMs. According to the geomorphic change detection analysis, the volume of the landslide was estimated to be  $7.70 \pm 1.46$  million  $m^3$ . An unstable mass approximately 500 m below the back edge of the

landslide was also identified based on the above analysis.

Moreover, a rapid assessment of the disaster was conducted based on high-resolution satellite images before the landslide and aerial images after the landslide, acquired from UAV. Constrained by the terrain conditions, the densely populated and more economically developed areas in the upper reaches of the Minjiang River basin are mainly located in the bottom of valleys. Such places are dangerous because of the landslide, debris flow and flash flood occurrence. Therefore it is important to carefully select residential sites to avoid such as a large number of casualties. The suggestion, based on the results, is to keep the traditional characteristics of the residents that include scattered and multi-point residences, rather than large concentrated settlements.

This study provides just a preliminary analysis on Xinmo landslide. However, it should be used as a useful support to the government to quickly visualize the disaster and plan emergency responses to reduce casualties and prevent serious secondary disasters.

### Acknowledgements

This research is funded by the National Key Research and Development Program of China (Grants No. 2017YFC0505104) and the Key Laboratory of Digital Mapping and Land Information Application of National Administration of Surveying, Mapping and Geoinformation of China (Grants No. DM2016SC09). The Sichuan Bureau of Surveying, Mapping and Geo-information (SBSMG) conducted the UAV survey and provided the terrain data and remote sensing images used in this study.

### References

- Calò F, Ardizzone F, Castaldo R, et al. (2014) Enhanced landslide investigations through advanced DInSAR techniques: The Ivancich case study, Assisi, Italy. *Remote Sensing of Environment* 142: 69-82. <https://doi.org/10.1016/j.rse.2013.11.003>
- Cui P, Chen XQ, Zhu YY, et al. (2011) The Wenchuan earthquake (May 12, 2008), Sichuan province, China, and resulting geohazards. *Natural Hazards* 56(1): 19-36. <https://doi.org/10.1007/s11069-009-9392-1>
- Cui P, Zhu YY, Han YS, et al. (2009) The 12 May Wenchuan earthquake-induced landslide lakes: distribution and preliminary risk evaluation. *Landslides* 6(3): 209-223. <https://doi.org/10.1007/s10346-009-0160-9>
- DeLong SB, Prentice CS, Hilley GE, et al. (2012) Multitemporal ALSM change detection, sediment delivery, and process mapping at an active earthflow. *Earth Surface Processes and Landforms* 37(3): 262-272. <https://doi.org/10.1002/esp.2234>
- Fan JR, Chen JX, Tian BW, et al. (2010) Rapid assessment of secondary disasters induced by the Wenchuan Earthquake. *Computing in science & engineering* 12(1): 10-19. <https://doi.org/10.1109/MCSE.2010.16>
- Fan JR, Li XZ, Guo FF, et al. (2011) Empirical-statistical models based on remote sensing for estimating the volume of landslides induced by the Wenchuan earthquake. *Journal of Mountain Science* 8(5): 711-717. <https://doi.org/10.1007/s11629-011-2133-4>
- Fan X, van Westen CJ, Korup O, et al. (2012) Transient water and sediment storage of the decaying landslide dams induced by the 2008 Wenchuan earthquake, China. *Geomorphology* 171: 58-68. <https://doi.org/10.1016/j.geomorph.2012.05.003>

- Fan YD, Wu W, Wang W, et al. (2016) Research progress of disaster remote sensing in China. *Journal of Remote Sensing* 20(05): 1170-1184. (In Chinese)
- Fang X, Pomeroy JW, Westbrook CJ, et al. (2010) Prediction of snowmelt derived streamflow in a wetland dominated prairie basin. *Hydrology and Earth System Sciences* 14(6): 991-1006. <https://doi.org/10.5194/hess-14-991-2010>
- Fang YP, Fan J, Shen MY, et al. (2014) Sensitivity of livelihood strategy to livelihood capital in mountain areas: Empirical analysis based on different settlements in the upper reaches of the Minjiang River, China. *Ecological Indicators* 38: 225-235. <https://doi.org/10.1016/j.ecolind.2013.11.007>
- Fiorucci F, Cardinali M, Carlà R, et al. (2011) Seasonal landslide mapping and estimation of landslide mobilization rates using aerial and satellite images. *Geomorphology* 129(1): 59-70. <https://doi.org/10.1016/j.geomorph.2011.01.013>
- Galli M, Ardizzone F, Cardinali M, et al. (2008) Comparing landslide inventory maps. *Geomorphology* 94(3): 268-289. <https://doi.org/10.1016/j.geomorph.2006.09.023>
- Guthrie RH, Evans SG. (2004) Analysis of landslide frequencies and characteristics in a natural system, coastal British Columbia. *Earth Surface Processes and Landforms* 29(11): 1321-1339. <https://doi.org/10.1002/esp.1095>
- Guzzetti F, Ardizzone F, Cardinali M, et al. (2009) Landslide volumes and landslide mobilization rates in Umbria, central Italy. *Earth and Planetary Science Letters* 279(3): 222-229. <https://doi.org/10.1016/j.epsl.2009.01.005>
- Guzzetti F, Carrara A, Cardinali M, et al. (1999) Landslide hazard evaluation: a review of current techniques and their application in a multi-scale study, Central Italy. *Geomorphology* 31(1): 181-216. [https://doi.org/10.1016/S0169-555X\(99\)00078-1](https://doi.org/10.1016/S0169-555X(99)00078-1)
- Imaizumi F, Sidle RC, Kamei R. (2008) Effects of forest harvesting on the occurrence of landslides and debris flows in steep terrain of central Japan. *Earth Surface Processes and Landforms* 33(6): 827-840. <https://doi.org/10.1002/esp.1574>
- Innes JL (1983) Lichenometric dating of debris - flow deposits in the Scottish Highlands. *Earth Surface Processes and Landforms* 8(6): 579-588. <https://doi.org/10.1002/esp.3290080609>
- Jaboyedoff M, Oppikofer T, Abellán A, et al. (2012) Use of LIDAR in landslide investigations: a review. *Natural Hazards* 61(1): 5-28. <https://doi.org/10.1007/s11069-010-9634-2>
- Koi T, Hotta N, Ishigaki I, et al. (2008) Prolonged impact of earthquake-induced landslides on sediment yield in a mountain watershed: the Tanzawa region, Japan. *Geomorphology* 101(4): 692-702. <https://doi.org/10.1016/j.geomorph.2008.03.007>
- Korup O (2005) Distribution of landslides in southwest New Zealand. *Landslides* 2(1): 43-51. <https://doi.org/10.1007/s10346-004-0042-0>
- Lin CW, Tseng CM, Tseng YH, et al. (2013) Recognition of large scale deep-seated landslides in forest areas of Taiwan using high resolution topography. *Journal of Asian Earth Sciences* 62: 389-400. <https://doi.org/10.1016/j.jseae.2012.10.022>
- Lucieer A, Jong SM, Turner D. (2014) Mapping landslide displacements using Structure from Motion (SfM) and image correlation of multi-temporal UAV photography. *Progress in Physical Geography* 38(1): 97-116. <https://doi.org/10.1177/0309133313515293>
- Nex F, Remondino F (2014) UAV for 3D mapping applications: a review. *Applied Geomatics* 6(1): 1-15. <https://doi.org/10.1007/s12518-013-0120-x>
- Ouyang CJ, Zhao W, He SM, et al. (2017) Numerical modeling and dynamic analysis of the 2017 Xinmo landslide in Maoxian County, China. *Journal of Mountain Science* 14(9). <https://doi.org/10.1007/s11629-017-4613-7>
- Passalacqua P, Hillier JH, Tarolli P. (2014) Innovative analysis and use of high resolution DTMs for understanding Earth-surface processes. *Earth Surface Processes and Landforms* 39(10): 1400-1403. <https://doi.org/doi:10.1002/esp.3616>
- Prosdociami M, Calligaro S, Sofia G, et al. (2015) Bank erosion in agricultural drainage networks: new challenges from structure-from-motion photogrammetry for post-event analysis. *Earth Surface Processes and Landforms* 40(14): 1891-1906. <https://doi.org/10.1002/esp.3767>
- Rice RM, Crockett ES, Bailey RG (1969) Soil slips related to vegetation, topography, and soil in southern California. *Water Resources Research* 5(3): 647-659. <https://doi.org/10.1029/WR005i003p0647>
- Santangelo M, Marchesini I, Cardinali M, et al. (2015) A method for the assessment of the influence of bedding on landslide abundance and types. *Landslides* 12(2): 295-309. <https://doi.org/10.1007/s10346-014-0485-x>
- Schlögel R, Doubre C, Malet JP, et al. (2015) Landslide deformation monitoring with ALOS/PALSAR imagery: a D-InSAR geomorphological interpretation method. *Geomorphology* 231: 314-330. <https://doi.org/10.1016/j.geomorph.2014.11.031>
- Siebert S, Teizer J (2014) Mobile 3D mapping for surveying earthwork projects using an Unmanned Aerial Vehicle (UAV) system. *Automation in Construction* 41: 1-14. <https://doi.org/10.1016/j.autcon.2014.01.004>
- Smith MW, Vericat D (2015) From experimental plots to experimental landscapes: topography, erosion and deposition in sub-humid badlands from structure-from-motion photogrammetry. *Earth Surface Processes and Landforms* 40(12): 1656-1671. <https://doi.org/10.1002/esp.3747>
- Stumpf A, Malet JP, Allemand P, et al. (2015) Ground-based multi-view photogrammetry for the monitoring of landslide deformation and erosion. *Geomorphology* 231: 130-145. <https://doi.org/10.1016/j.geomorph.2014.11.039>
- Su LJ, Hu KH, Zhang WF, et al. (2017) Characteristics and triggering mechanism of Xinmo landslide on 24 June 2017 in Sichuan, China. *Journal of Mountain Science* 14(9). <https://doi.org/10.1007/s11629-017-4609-3>
- Tachikawa T, Hato M, Kaku M, et al. (2011) Characteristics of ASTER GDEM version 2. IEEE International Geoscience and Remote Sensing Symposium (IGARSS), Vancouver, BC, 2011, pp. 3657-3660. <https://doi.org/10.1109/IGARSS.2011.6050017>
- Tang C, Rengers N, Van Asch TWJ, et al. (2011) Triggering conditions and depositional characteristics of a disastrous debris flow event in Zhouqu city, Gansu Province, northwestern China. *Natural Hazards and Earth System Sciences* 11(11): 2903-2912. <https://doi.org/10.5194/nhess-11-2903-2011>
- Tarolli P. (2014) High-resolution topography for understanding earth surface processes: Opportunities and challenges. *Geomorphology* 216: 295-312. <https://doi.org/10.1016/j.geomorph.2014.03.008>
- Tarolli P, Sofia G, Dalla Fontana G (2012) Geomorphic features extraction from high-resolution topography: landslide crowns and bank erosion. *Natural Hazards* 61(1): 65-83. <https://doi.org/10.1007/s11069-010-9695-2>
- Tseng CM, Chang KJ, Tarolli P. (2017) The Sediment Production and Transportation in a Mountainous Reservoir Watershed, Southern Taiwan. In: Mikoš M, Vilímek V, Yin Y, Sassa K (eds) *Advancing Culture of Living with Landslides*. WLF 2017. 291-299. aSpringer, Cham. [https://doi.org/10.1007/978-3-319-53483-1\\_34](https://doi.org/10.1007/978-3-319-53483-1_34)
- Tseng CM, Lin CW, Dalla Fontana G, Tarolli P. (2015) The topographic signature of a major typhoon. *Earth Surface Processes and Landforms* 40: 1129-1136. <https://doi.org/doi:10.1002/esp.3708>
- Tseng CM, Lin CW, Stark CP, et al. (2013) Application of a multi-temporal, LiDAR-derived, digital terrain model in a landslide-volume estimation. *Earth Surface Processes and Landforms* 38(13): 1587-1601. <https://doi.org/10.1002/esp.3454>
- Turner D, Lucieer A, De Jong SM (2015) Time series analysis of landslide dynamics using an unmanned aerial vehicle (UAV). *Remote Sensing* 7(2): 1736-1757. <https://doi.org/10.3390/rs70201736>
- Wang F, Cheng Q, Highland L, et al. (2009) Preliminary investigation of some large landslides triggered by the 2008 Wenchuan earthquake, Sichuan Province, China. *Landslides* 6(1): 47-54. <https://doi.org/10.1007/s10346-009-0141-z>
- Wang K, Shen ZK (2011) Location and focal mechanism of the 1933 Diexi earthquake and its associated regional tectonics. *Acta Seismologica Sinica* 33(5): 557-567. (In Chinese)
- Wheaton JM, Brasington J, Darby SE, et al. (2010) Accounting for uncertainty in DEMs from repeat topographic surveys: improved sediment budgets. *Earth Surface Processes and Landforms* 35(2): 136-156. <https://doi.org/10.1002/esp.1886>
- Xu Q, Fan XM, Huang RQ, et al. (2009) Landslide dams triggered by the Wenchuan Earthquake, Sichuan Province, south west China. *Bulletin of engineering geology and the environment* 68(3): 373-386. <https://doi.org/10.1007/s10064-009-0214-1>
- Xu Q, Li WL (2010) Distribution of large scale landslides induced by the Wenchuan earthquake. *Journal of Engineering Geology* 18(6): 818-826. (In Chinese)